Title

The synthetic diazonamide DZ-2384 has distinct effects on microtubule curvature and dynamics without neurotoxicity

Journal

Science Translational Medicine, 8(365)

ISSN

1946-6234

Authors

Wieczorek, Michal
Tcherkezian, Joseph
Bernier, Cynthia
et al.

Publication Date

2016-11-16

DOI

10.1126/scitranslmed.aag1093

Peer reviewed

HHS Public Access

Author manuscript

Sci Transl Med. Author manuscript; available in PMC 2017 November 16.

Published in final edited form as:

Sci Transl Med. 2016 November 16; 8(365): 365ra159. doi:10.1126/scitranslmed.aag1093.

The synthetic diazonamide DZ-2384 has distinct effects on microtubule curvature and dynamics without neurotoxicity

Michal Wieczorek[1], **Joseph Tcherkezian**[2], **Cynthia Bernier**[2], **Andrea E. Prota**[3], **Sami Chaaban**[1], **Yannève Rolland**[2], **Claude Godbout**[2], **Mark A. Hancock**[4], **Joseph C. Arezzo**[5], **Ozhan Ocal**[6], **Cecilia Rocha**[1], **Natacha Olieric**[3], **Anita Hall**[7,8], **Hui Ding**[9], **Alexandre Bramoullé**[2], **Matthew G. Annis**[7], **George Zogopoulos**[7,8], **Patrick G. Harran**[9], **Thomas M. Wilkie**[6], **Rolf A. Brekken**[6], **Peter M. Siegel**[7], **Michel O. Steinmetz**[3], **Gordon C. Shore**[2], **Gary J. Brouhard**[1,*], and **Anne Roulston**[2,*]

[1]Department of Biology, McGill University, Montreal, Quebec H3A 1B1, Canada [2]Laboratory for Therapeutic Development, Rosalind and Morris Goodman Cancer Research Centre and Department of Biochemistry, McGill University, Montreal, Quebec H3G 1Y6, Canada [3]Laboratory of Biomolecular Research, Department of Biology and Chemistry, Paul Scherrer Institut, 5232 Villigen PSI, Switzerland [4]McGill SPR-MS Facility, McGill University, Montreal, Quebec H3G 1Y6, Canada [5]Department of Neuroscience, Albert Einstein College of Medicine, Bronx, NY 10561, USA [6]Department of Pharmacology, UT Southwestern Medical Center, Dallas, TX 75390, USA [7]Rosalind and Morris Goodman Cancer Research Centre, McGill University, Montreal, Quebec H3A 1A3, Canada [8]Research Institute of the McGill University Health Centre, Montreal, Quebec H4A 3J1, Canada [9]Department of Chemistry and Biochemistry, University of California at Los Angeles, Los Angeles, CA 90095, USA

Abstract

Microtubule-targeting agents (MTAs) are widely used anticancer agents, but toxicities such as neuropathy limit their clinical use. MTAs bind to and alter the stability of microtubules, causing cell death in mitosis. We describe DZ-2384, a preclinical compound that exhibits potent antitumor

[*]Corresponding author. gary.brouhard@mcgill.ca (G.J.B.); anne.roulston@mcgill.ca (A.R.).

Author contributions: M.W., J.T., C.B., A.E.P., Y.R., M.A.H., J.C.A., O.O., G.Z., P.G.H., M.O.S., T.M.W., R.A.B., P.M.S., G.C.S., G.J.B., and A.R. designed research studies; M.W., J.T., C.B., A.E.P., S.C., Y.R., C.G., M.A.H., J.C.A., O.O., C.R., N.O., H.D., M.G.A., and A.H. conducted experiments; M.W., J.T., C.B., A.E.P., S.C., Y.R., C.G., M.A.H., J.C.A., O.O., C.R., N.O., A.B., M.G.A., M.O.S., T.M.W., G.C.S., G.J.B., and A.R. analyzed data; and M.W., J.T., C.B., A.E.P., M.A.H., J.C.A., M.O.S., T.M.W., P.G.H., G.C.S., G.J.B., and A.R. wrote or edited the manuscript.

Competing interests: Diazon Pharmaceuticals Inc. holds the rights to the Patent Cooperation Treaty publication no. WO2009/134938 that covers DZ-2384. None of the authors of this manuscript are named inventors on this patent. G.C.S., A.R., and P.H. are founders and shareholders in Diazon Pharmaceuticals Inc. R.A.B. and T.M.W. are founders of Tuevol Therapeutics Inc. and are inventors on patent applications (62/067,304; 62/067,276; 62/232,901; and 62/232,922) held or submitted by the UT Southwestern Medical Center that cover the use of the GEMM rapid in vivo assay (*Rgs16::GFP;KIC* model) for screening therapeutics for pancreatic ductal adenocarcinoma.

Data and materials availability: Coordinates have been deposited in the Protein Data Bank (PDB) under accession no. 5LOV (DZ-2384–tubulin complex).

SUPPLEMENTARY MATERIALS

www.sciencetranslationalmedicine.org/cgi/content/full/8/365/365ra159/DC1

Materials and Methods

References (63–77)

activity in models of multiple cancer types. It has an unusually high safety margin and lacks neurotoxicity in rats at effective plasma concentrations. DZ-2384 binds the vinca domain of tubulin in a distinct way, imparting structurally and functionally different effects on microtubule dynamics compared to other vinca-binding compounds. X-ray crystallography and electron microscopy studies demonstrate that DZ-2384 causes straightening of curved protofilaments, an effect proposed to favor polymerization of tubulin. Both DZ-2384 and the vinca alkaloid vinorelbine inhibit microtubule growth rate; however, DZ-2384 increases the rescue frequency and preserves the microtubule network in nonmitotic cells and in primary neurons. This differential modulation of tubulin results in a potent MTA therapeutic with enhanced safety.

INTRODUCTION

Microtubules are essential in rapidly dividing cells where they form the mitotic spindle, an apparatus that ensures proper chromosome segregation during mitosis (1, 2). As such, microtubules are the direct target of a large group of chemotherapeutics, known as microtubule-targeting agents (MTAs), that effectively kill cancer cells as they divide [reviewed in (3)]. MTAs can bind to five distinct sites on tubulin, with the taxane site and the vinca alkaloid site being the most prominent targets. Although different MTAs bind to distinct sites, cancer cell death occurs by a similar mechanism with all of them: an arrest in mitosis causes prolonged activation of the spindle assembly checkpoint, which ultimately triggers apoptosis (4, 5).

Despite the success of MTAs in the clinic, toxic side effects often force discontinuation of treatment or reduction in dose. The most common problems are neutropenia (6) and peripheral neuropathy (7). The latter can be especially severe when MTAs are combined with other chemotherapeutics such as cisplatin or bortezomib, a common practice (8). Because microtubules are the backbone of neurons, it is not surprising that MTAs would cause neuropathy, particularly in the peripheral nerves that have the longest axons (9). Nerve degeneration often persists well beyond the treatment period, and some patients never fully recover from the damage (10). There is a pressing need for improved, less toxic MTAs, which would enable sustained treatments, combine well with other therapies, and reduce neuropathy.

MTAs function largely by altering the dynamics and stability of microtubules. Microtubules are polymers of αβ-tubulin heterodimers, which associate head-to-tail to form protofilaments and then laterally to form a tube. Current MTAs such as paclitaxel stabilize these polymers, whereas MTAs such as vinblastine and vinorelbine destabilize them. More specifically, vinca alkaloids destabilize microtubules by introducing a wedge at the interface between two longitudinally aligned tubulin dimers, thus inhibiting the interdimer curved-to-straight transition that is necessary to build the microtubule lattice. Microtubules polymerize by the addition of tubulin to the microtubule end, which is a tapered, gently curved, and flattened-out polymer structure (11). As the microtubule grows, the protofilaments straighten (12), forming lateral bonds with adjacent protofilaments within the microtubule lattice. Abruptly, the polymer switches from growth to shrinkage in a “catastrophe” (13–15). As the microtubule shrinks, individual protofilaments lose their lateral contacts and curve outward

steeply (1). Sporadically, the rapidly shrinking microtubule will switch back to growth in a "rescue" event. Understanding the mechanism of MTAs has contributed substantially to the fundamental principles of microtubule dynamics (16, 17). An MTA that changes microtubule dynamics differently from others, even subtly, could prove more effective at arresting cells in mitosis without disrupting microtubule function in nondividing cells.

Many MTAs are natural products or chemically modified analogs of natural products (3). Diazonamide A (DZA) is a natural product originally isolated from the marine sponge *Diazona angulata* (18, 19). DZA was initially modified into the synthetic analog AB-5, which showed encouraging antitumor activity in xenograft models (20). Here, we present DZ-2384, an optimized synthetic derivative of AB-5, which is in preclinical development. Relative to earlier diazonamide analogs, its synthesis is simplified and commercially scalable (21). DZ-2384 shows potent antitumor activity in multiple cancer models but causes negligible side effects (including neuropathy) at effective plasma concentrations. We demonstrate that DZ-2384 binds to the vinca alkaloid site of tubulin in a distinctive way that unexpectedly translates into superior antitumor efficacy and safety. Using x-ray crystallography and electron microscopy (EM), we show that DZ-2384 changes the curvature between two tubulin dimers, causing a pronounced straightening of protofilaments. In live cells, DZ-2384 increases the rescue frequency and has a less destabilizing effect on microtubules than vinorelbine yet is sufficiently potent to disrupt mitotic spindle formation. We observed similar effects in a reconstituted system using purified tubulin. We propose that structural differences between DZ-2384 and vinca alkaloids correlate with a milder impact on interphase microtubules and the absence of peripheral neuropathy at effective plasma concentrations. Our results demonstrate that a classic therapeutic site on tubulin can be targeted in a different way, resulting in a potent yet less toxic candidate MTA for chemotherapy.

RESULTS

DZ-2384 has potent antitumor activity in multiple disease models

To establish the in vivo antitumor efficacy of DZ-2384, we tested it along with vinorelbine in two subcutaneous xenograft models, namely, the MIA PaCa-2 model of pancreatic ductal adenocarcinoma (PDAC or PDA) and the HT-29 model of colon cancer. DZ-2384 was highly effective in both models (Fig. 1A and table S1). DZ-2384 caused complete tumor regression in the MIA-PaCa-2 model and, at 9 mg/m^2, all mice were tumor-free ~3 months after treatment (Fig. 1A). Vinorelbine was also active in both models, but at higher doses and for a shorter duration (Fig. 1B and table S1). Table 1 summarizes the minimum effective dose (MED) for both DZ-2384 and vinorelbine in the MIA PaCa-2 and HT-29 models.

We also tested the efficacy of DZ-2384 in an experimental model of metastatic triple-negative breast cancer (MDA-MB-231-LM2), which recapitulates the later stages of the metastatic cascade (22). We injected MDA-MB-231-LM2 cells into the tail vein of severe combined immunodeficient (SCID)/beige mice, allowed lung metastatic lesions to develop, and then treated the mice with DZ-2384. DZ-2384 caused regression of all lung metastases starting at the lowest dose tested (Fig. 1C and fig. S1A) and significantly increased the survival of all DZ-2384–treated groups ($P < 0.0001$; Fig. 1D). Some animals were tumor-

free up to 106 days after initial treatment (2 of 8 mice at 18 mg/m^2 and 1 of 5 mice at 4.5 mg/m^2).

Finally, we tested DZ-2384 in the RS4;11 model of adult Philadelphia chromosome–negative acute lymphocytic leukemia (ALL). DZ-2384 reduced the number of tumor cells in circulation on day 23 ($P = 0.0028$) and increased survival ($P = 0.0024$) at doses as low as 0.7 mg/m^2 (fig. S1, B and C). In each of the xenograft models described above, the mice experienced less than 10% body weight loss at all DZ-2384 and vinorelbine doses tested (fig. S2, A to F). Together, these results demonstrate that DZ-2384 is potent against tumors in human xenograft models of several different tumor types.

DZ-2384 enhances gemcitabine activity in two mouse models of pancreatic cancer

Our results in the MIA PaCa-2 model were encouraging because patients with PDA continue to have very low survival rates. Treatment options are limited, but the MTA nanoparticle albumin-bound (nab)–paclitaxel was recently approved for use in combination with gemcitabine in the metastatic setting, indicating that MTAs can improve the outcome of PDA (23). We sought to determine whether DZ-2384 is effective in two rigorous in vivo models of pancreatic cancer, either alone or in combination with gemcitabine. In a patient-derived xenograft (PDX) model, we propagated tumors in SCID/beige mice to obtain a large cohort of tumor-bearing animals for treatment. Whereas either gemcitabine or DZ-2384 used as single agents had insignificant effects on tumor growth, the combination of DZ-2384 and gemcitabine (DZ-2384/gemcitabine) caused significant ($P = 0.0159$) tumor regression (Fig. 1E). The mice lost 11% of their body weight after the first dose of DZ-2384 and DZ-2384/gemcitabine but then quickly recovered (fig. S2G). One animal inexplicably died in the DZ-2384–treated group on day 29, whereas viability was 100% in the DZ-2384/gemcitabine–treated group for the duration of the experiment.

Next, we tested DZ-2384 and gemcitabine in a genetically engineered mouse model (GEMM) of PDA, specifically *KIC* [*p48(Cre)*; *LSL-Kras (G12D)*; *Cdkn2a(f/f)*] mice that express Rgs16::GFP as a fluorescent marker to assess tumor burden (24). Mice were treated with single-agent gemcitabine or with DZ-2384/gemcitabine from postnatal day 15 (P15) until they are sacrificed on P29 (Fig. 1F). Tumor burden was quantified by green fluorescent protein (GFP) intensity of micrographs taken from the five brightest fields of dissected pancreata (24). The absence of observed GFP in several micrographs from mice treated with DZ-2384/gemcitabine relative to untreated mice or mice treated with single-agent gemcitabine indicates fewer PDA initiation sites and a higher frequency of mice with negligible or greatly reduced tumor burden (Fig. 1G). The response rate (reduction in GFP fluorescence intensity) more than doubled with the DZ-2384 and gemcitabine combination relative to gemcitabine alone. Mild hair loss, diarrhea, and hindlimb paralysis were observed in weanling mice with DZ-2384/gemcitabine but not with gemcitabine alone (table S2). DZ-2384–related toxicity was age-dependent in that DZ-2384 doses of 30 mg/m^2 were tolerated when administered on P23 (no mortality; table S2) but not on P16 (table S3). We did not observe weight loss, but growth delay was experienced by DZ-2384/gemcitabine–treated weanling mice during the experiment (figs. S2H and S3). Together, these results

provide a rationale for the combined use of DZ-2384 and gemcitabine in the treatment of pancreatic cancer.

DZ-2384 has a wide safety margin compared to vinorelbine

To establish the safety and tolerability of DZ-2384 and vinorelbine in mice, we conducted toxicity studies to determine the no observable adverse effect level (NOAEL; dose at which animals showed minimal weight loss and no bone marrow toxicity) (tables S4 and S5 for DZ-2384 and vinorelbine, respectively). Then, the safety margin was determined on the basis of compound exposure. For this, we measured the systemic concentrations of each compound by liquid chromatography–tandem mass spectrometry analysis in plasma over time at selected doses representing their MEDs (determined in the Mia PaCa-2 and HT-29 models) and NOAELs. The results are presented in Table 1. Comparing compound exposure (plasma AUC) at the MED to exposure at NOAEL yields a safety margin for DZ-2384 of 24.4 to 53.5. The safety margins for vinorelbine are 0.7 to 1.0 in the same models. We conclude that DZ-2384 has a much wider safety margin than vinorelbine.

DZ-2384 lacks neurotoxicity at effective doses

Damage to peripheral neurons often limits the use of MTAs in the clinic (25, 26). Sprague-Dawley rats treated with DZ-2384 were evaluated for evidence of peripheral neuropathy by measuring nerve conduction velocity (NCV) and onset latency in the caudal nerve, the distal digital nerve, and the motor branch of the tibial nerve. These nerves include sensory axons (distal digital), motor axons (tibial), and mixed sensory, motor, and autonomic fibers (caudal). A decrease in NCV or an increase in onset latency is evidence of impaired neuronal function. Animals were exposed to either DZ-2384 or docetaxel, an MTA that is known to cause peripheral neuropathy. Each compound was delivered once weekly over a 4-week period at doses up to and including the maximum tolerated dose (MTD) as determined by death rate or >20% body weight loss. The MTDs for DZ-2384 and docetaxel were 30 and 120 mg/m^2, respectively (fig. S4). NCV and onset latency were recorded before treatment, 2 days after the fourth dose (day 24), and 3 weeks after the fourth dose (day 44).

As expected, docetaxel at 120 mg/m^2 caused a decrease in NCV in caudal and digital nerves and an increase in onset latency in tibial nerves on day 24 (Fig. 2, A to C). After the 22-day recovery period, there was no improvement in either caudal or digital NCV; however, there was a slight improvement in tibial motor latency. Histology of the docetaxel-treated animals on day 44 showed incomplete recovery of the damaged dorsal root ganglia (Fig. 2D) and peripheral (sciatic) nerves (Fig. 2E), indicated by the presence of degenerating neurons with condensed nuclei and digestion chambers filled with myelin debris.

DZ-2384 was tested in rats at 12 mg/m^2 (more than two times higher than its MED in mouse xenograft models) and at 30 mg/m^2 (MTD). On day 24, normal NCV and onset latency were observed in rats exposed to DZ-2384 at 12 mg/m^2 relative to age-matched controls (Fig. 2, A to C). Histology performed on day 44 showed no changes in the lumbar dorsal root ganglia or in the sciatic nerve (Fig. 2, D and E). At 30 mg/m^2, the tibial nerve was unaffected; however, a slowing of the caudal and distal digital NCV was observed, although the decrease was smaller than that for docetaxel. At this dose level, the NCV remained slow on day 44

(Fig. 2, A to C). At the end of the recovery period, we did not find histological evidence of neurotoxicity in the dorsal root ganglia or sciatic nerve (Fig. 2, D and E), suggesting a substantial degree of recovery, although the distal axons were not examined. Histopathology data are summarized in table S6.

To relate DZ-2384 neurotoxicity in rats to exposure (AUC) levels that are effective in mouse tumor models, we measured the pharmacokinetics of DZ-2384 in Sprague-Dawley rats. At 12 mg/m^2, where no neuropathy was seen, the rat AUC was 4371 ng·hour/ml, which is 13-to 28-fold higher than plasma levels that are effective in mouse xenograft models (Table 1). These data indicate that DZ-2384 does not cause neuropathy at doses that are highly effective in multiple cancer models.

Functional genomics points to an antimitotic mechanism of action

Identifying the cellular target of diazonamides has been challenging. One candidate is the mitochondrial enzyme ornithine δ-aminotransferase, which was identified by binding interactions (27), whereas other studies have implicated microtubules (28). To interrogate the mechanism of action without bias, we performed a genome-wide RNA interference screen in H1299 cells to uncover genes that confer either sensitivity or resistance on DZ-2384. Half maximal growth inhibitory concentration (IC_{50}) values for DZ-2384 were calculated with each test small interfering RNA (siRNA) pool relative to nontargeting siRNA controls. We identified 631 sensitizer genes and 179 resistor genes, defined as siRNA pools that shifted the IC_{50} for DZ-2384 by >2 SD from the mean of all data points (fig. S5A). To determine the major pathways that conferred sensitivity or resistance and hence the potential mechanism of action, we performed pathway analysis of the hits. Of the top 10 most highly represented pathways, 6 were related to cell cycle, mitosis, and microtubules (fig. S5B). To confirm mitotic arrest and apoptosis, we treated H1299 cells with DZ-2384 for 48 hours and measured their DNA content and caspase-3 activation. DZ-2384–treated cells accumulated in the G2-M phase of the cell cycle starting at 4 to 8 hours (fig. S5, C to F) and began to undergo apoptosis at 16 hours after treatment as demonstrated by procaspase-3 cleavage (fig. S5G). Combined with the results of the RNA interference screen, these results suggested that DZ-2384 acts as an antimitotic agent (5).

DZ-2384 binds to the vinca alkaloid site of tubulin

To investigate whether DZ-2384 binds to tubulin directly, we used surface plasmon resonance (SPR) to detect binding between biotinylated DZ-2384, which was immobilized to streptavidin-coated sensors, and purified tubulin dimers. We observed dose-dependent increases in the SPR signal when tubulin was titrated in single-cycle kinetics mode (Fig. 3A). As negative controls, neither actin nor bovine serum albumin (BSA) bound to biotinylated DZ-2384 surfaces, nor did tubulin bind to surfaces coated with streptavidin only or with a biotinylated inactive diastereomer of DZ-2384 (DZ-2384D; fig. S6). As expected, preincubating tubulin with DZ-2384 inhibited its binding to biotinylated DZ-2384 surfaces (Fig. 3B), but similar incubations with DZ-2384D did not (Fig. 3C). To determine whether DZ-2384 binds to other MTA-tubulin binding sites in solution, we evaluated binding to the biotinylated DZ-2384 surface in the presence of vinorelbine. Preincubating tubulin with increasing concentrations of vinorel-bine blocked its binding to biotinylated DZ-2384

surfaces in a dose-responsive manner (Fig. 3D), suggesting that DZ-2384 binds at or near the vinca binding site.

To gain a more detailed view of the DZ-2384–tubulin binding site, we used a protein complex consisting of two αβ-tubulin dimers (T_2), the stathmin-like protein RB3 (R), and tubulin tyrosine ligase (TTL; the full complex is denoted as T_2R-TTL) (16, 29), and the structure of ligand-bound DZ-2384 (DZ-2384–T_2R-TTL) was solved to a resolution of 2.4 Å using x-ray crystallography. In the structure, DZ-2384 binds with a distinct binding mode (see the next section) to tubulin at the classic vinca alkaloid site, which lies at the longitudinal interface between the b subunit of one tubulin (β1 of T_2R-TTL) and the a subunit of the tubulin above it (α2 of T_2R-TTL) (Fig. 3, E and F, and fig. S7). Overall, these results establish DZ-2384 as an MTA that binds to the vinca site on tubulin. To determine the consequences of DZ-2384 biotinylation for tubulin binding, we modeled our biotin-linker DZ-2384 derivative onto the DZ-2384–T_2R-TTL complex (fig. S8). Because no structural rearrangements of the tubulin molecules are required to accommodate biotin-linker DZ-2384, and no clashes between the biotin-linker moiety and tubulin were observed, we conclude that the biotinylation of DZ-2384 does not affect binding to tubulin.

Our DZ-2384–tubulin structure also allowed us to explore the difference between DZ-2384 and its inactive diastereomer DZ-2384D. The structure of DZ-2384D was modeled into the binding pocket on tubulin by keeping the core interaction stationary and changing only the stereocenters of the indoline moiety. The model revealed that a large hydrophobic contact is missing in the diastereomeric ligand, namely, the contact formed by the fluorinated indoline moiety of DZ-2384 with loop T7, helix H10, and strand S9 of α2-tubulin (Fig. 3, F and G). This missing contact provides a structural explanation for the lack of tubulin binding by the diastereomer in the competitive SPR binding assay (Fig. 3, B and C).

DZ-2384 causes a change in curvature of tubulin protofilaments

Given that DZ-2384 has a wider safety margin than vinorelbine, we explored how DZ-2384 differs from other vinca alkaloid binding compounds. We began with a closer investigation of the DZ-2384–T_2R-TTL crystal structure described above. The DZ-2384 binding site is shaped by (i) the hydrophobic and polar residues of loop T7, helix H10, and strand S9 of α2-tubulin; (ii) the N-terminal residues of both helices H6 and H7; and (iii) the loops T5 and H6-H7 of β1-tubulin. In the DZ-2384–tubulin complex, the hydrophobic interactions with the secondary structural elements of α- and β-tubulin described above are complemented by direct and water-mediated hydrogen bonds to main-chain atoms of both tubulin subunits (Fig. 3E). Moreover, the two oxazole rings form a π-stacking interaction with the aromatic side chain of Tyr^{224} and the nucleotide of β1-tubulin.

To understand how DZ-2384 differs from other vinca alkaloids, we superimposed atomic models of tubulin in complex with DZ-2384 and vinblastine (Fig. 3H) (17). The superposition shows that DZ-2384 and vinblastine exploit the same hydrophobic pocket of α2-tubulin with their corresponding indoline moieties, and both molecules are involved in the same π-stacking interaction (bottom dashed circle in Fig. 3H). In other words, both molecules share a similar space at the interdimer interface. The exception is the bulky moiety from the catharanthine nucleus in vinblastine, which is common in vinca alkaloids

(30). This catharanthine nucleus is missing in DZ-2384. As a consequence, the intertubulin dimer interface in the DZ-2384–T_2R-TTL complex is more compact compared to both the apo–T_2R-TTL and vinblastine–T_2R-TTL complexes (Fig. 4A). The compactness in turn causes an overall change in the relative orientation of the two tubulin dimers in the DZ-2384–T_2R-TTL complex compared to the corresponding orientation observed for the vinblastine–T_2R-TTL [Protein Data Bank (PDB) ID 5J2T] and the apo–T_2R-TTL (PDB ID 4I55) complexes (Fig. 4A). To quantitatively evaluate this change, we analyzed helical superassemblies of different T_2R-TTL complexes as described previously (31). We estimated radii and pitches of 210, 180, and 250 Å and 250, 340, and −80 Å for apo–T_2R-TTL, vinblastine–T_2R-TTL, and DZ-2384–T_2R-TTL, respectively (Fig. 4B). On the basis of the increased radii of DZ-2384–T_2R-TTL, we hypothesize that DZ-2384 can unbend curved protofilaments to bring them conformationally closer to the straight protofilaments of microtubule shafts.

Vinca alkaloids stabilize curved, ring-like oligomers of tubulin at high concentrations (17). To determine whether DZ-2384 changes the pitch and curvature of these oligomers, we polymerized tubulin in the presence of DZ-2384 or vinblastine. Electron micrographs of crudely purified tubulin illustrate the decrease in pitch of protofilaments formed in the presence of DZ-2384 compared to that of vinblastine (Fig. 4C). To measure the curvature of such curved protofilaments, we polymerized highly purified tubulin with either DZ-2384 or vinblastine, mounted the polymers on EM grids, and measured them using custom software (Fig. 4D). Because the lengths of protofilaments induced by each compound were equivalent (fig. S9), we infer that they have a similar orientation on the grid surface. Therefore, the curvature measured in this way is representative of the actual radius of the tubulin-compound structures. As predicted by the crystal structure, the DZ-2384–induced protofilaments were straighter than those obtained with vinblastine [lower values for curvature (κ); Fig. 4E]. Together, the x-ray crystallography and EM demonstrate that DZ-2384 differs from vinblastine by changing the pitch and curvature of protofilaments.

Given that many of our experiments have used vinorelbine rather than vinblastine, we modeled the structure of vinorelbine into the vinca binding site. In our model, the catharanthine nuclei of vinorelbine and vinblastine heavily overlap (fig. S10); thus, we do not expect a difference in the change in protofilament curvature between these two agents. We note that vinblastine has two additional major hydrogen bonds to tubulin compared to vinorelbine, providing an explanation for the reported lower affinity of vinorelbine compared to vinblastine (32).

DZ-2384 has a milder effect on interphase and mitotic microtubule networks than vinorelbine

Although DZ-2384 induces mitotic arrest and triggers apoptosis, its wider safety margin suggests that it might have milder effects on microtubules in cells that are not actively undergoing mitosis. To test this idea, we used DZ-2384 and vinorelbine on a variety of cultured cells and assayed the integrity of their microtubule networks. H1299 cells weretreated with various concentrations of DZ-2384, DZ-2384D, vinorelbine, or docetaxel (Fig. 5A). In a microtubule sedimentation assay, a decrease in microtubule polymer mass

was observed with increasing DZ-2384 concentrations (but not with DZ-2384D), like with vinorelbine. However, despite having equivalent sensitivity to DZ-2384 and vinorelbine (IC_{50} values of 12 and 15 nM, respectively), H1299 cells treated with DZ-2384 maintained microtubule polymer mass at higher concentrations than those treated with vinorelbine. These differences indicate that DZ-2384 has a milder effect on the microtubule cytoskeleton in interphase cells. As a control, docetaxel increased microtubule polymer mass, as expected (3).

Next, we examined the effects of DZ-2384 on microtubules in actively dividing cells directly by confocal microscopy. HeLa cells were synchronized in late G2 with RO-3306 (a reversible cyclin-dependent kinase 1 inhibitor) (33) and released in the presence of equipotent concentrations of DZ-2384 (4 nM) or vinorelbine (11 nM), representing the IC_{80} of each compound in a 3-day cell viability assay. Synchronized cells released in the absence of compound show that microtubules form the appropriate spindle on which chromosomes are aligned in metaphase. DZ-2384–treated cells (Fig. 5B) show the presence of mostly bipolar spindles with stunted microtubules and visibly misaligned chromosomes. Similar results were obtained in H1299 cells (fig. S11). At equipotent concentrations, vinorelbine-treated cells lacked any detectable spindle microtubules in both cell lines (Fig. 5B and fig. S11). These findings suggest that although DZ-2384 has milder effects on mitotic spindles, these effects are still sufficient to interfere with cell division.

Similarly, unsynchronized U-2 OS osteosarcoma cells in interphase were treated with equipotent concentrations (3-day IC_{80}) of DZ-2384 and vinorelbine. In DZ-2384–treated cells, microtubules were present, although they were less dense at the cell periphery (Fig. 5C). In vinorelbine-treated cells, intact microtubules were difficult to observe, consistent with the loss of polymer mass observed in the pelleting assay above.

Finally, the effect of the two compounds on primary rat cortical neurons was assessed after 1 hour of treatment with 0.3 to 100 nM of each compound. Neurons treated with DZ-2384 up to 100 nM showed minimal qualitative differences compared to control-treated neurons in terms of axonal morphology, width, or intensity of tubulin staining (Fig. 5D and fig. S12). However, vinorelbine treatment produced thinner and/or fragmented axons starting at 0.3 nM and an overall reduction in tubulin staining intensity (Fig. 5D and fig. S12). Collectively, these results indicate that DZ-2384 has a milder effect on both interphase and mitotic microtubule networks than vinorelbine.

DZ-2384 has a distinct impact on microtubule dynamic instability

The milder impact of DZ-2384 on microtubules in cells suggests that DZ-2384 causes distinct changes in the dynamic instability of microtubules. To determine how DZ-2384 changes dynamic instability, we visualized growing ends of microtubules in U-2 OS cells stably expressing an EB3-mCherry fusion protein, which serves as a marker for growing ends (34). The cells were treated with DZ-2384 and vinorelbine at equipotent (IC_{80}) concentrations. In untreated cells, microtubule growth originates from the centrosome and radiates outward (movie S1). DZ-2384 treatment decreased the number of growing microtubules and the frequency with which they originate from the centrosome (movie S2),

as expected for a microtubule destabilizing agent. Vinorelbine treatment, however, had a more marked effect, vastly decreasing the number of growing microtubules (movie S3).

To more precisely measure the effect of DZ-2384 on dynamic instability, we imaged LLC-PK1 cells expressing GFP–α-tubulin (35), which allowed us to measure the growth rates, shrinkage rates, catastrophe (change from pause or growth to shrinkage) frequencies, and rescue (change from shrinkage to growth or pause) frequencies of dynamic microtubules. We compared the effects of DZ-2384 and vinorelbine, each at IC_{80} concentrations. Both DZ-2384 and vinorelbine reduced the microtubule growth rate and dynamicity equally (Table 2), and neither compound changed the shrinkage rate. DZ-2384 was distinguished from vinorelbine by an increased rescue frequency relative to control cells. Microtubules in vinorelbine-treated cells also spent a higher proportion of time in a paused state and less (3×) time in a growth state compared to those in DZ-2384–treated or control cells. Overall, these results explain the greater integrity of the microtubule network in cells treated with DZ-2384 compared to vinorelbine. Although DZ-2384 may cause microtubules to grow more slowly, the increase in rescue events compensates and helps to maintain tubulin in the polymeric state. However, during mitosis, DZ-2384's decreased growth rate is sufficient to disrupt the mitotic spindle, sending cells into growth arrest.

DZ-2384 increases microtubule rescues in a reconstituted system

Cells contain dozens of microtubule-associated proteins (MAPs) that regulate microtubule dynamics, including rescue frequency and growth rate. Therefore, we cannot conclude from cell-based studies whether DZ-2384 affects dynamic instability directly through interactions with tubulin or indirectly through MAPs. To determine whether the change in rescue frequency that we observed in DZ-2384–treated cells also occurs in a purified system in the absence of MAPs, we reconstituted microtubule growth in vitro using the single molecule assay for microtubule dynamics (36). Microtubule seeds stabilized by guanosine-5′-[(a,b)-methyleno]triphosphate were adhered to the surface of a flow chamber, and fluorescently labeled tubulin was introduced (Fig. 6A). We generated kymographs of growing microtubules in the presence of increasing concentrations of either DZ-2384 or vinorelbine (Fig. 6, B to D) and measured microtubule dynamics. Consistent with the growth inhibition seen in LLC-PK1 cells, DZ-2384 strongly affected microtubule dynamics; at 100 nM DZ-2384, the growth and shrinkage rates decreased by about twofold (Fig. 6, E and F) relative to untreated microtubules, and catastrophe frequencies were slightly increased (Fig. 6G). Comparable growth and shrinkage rate decreases were observed with vinorelbine and were consistent with previous reports (37, 38). We attribute the differences between the single-molecule assay and in-cell measurements to the absence of MAPs in our reconstituted system. Strikingly, however, DZ-2384 increased the rescue frequency in the reconstituted system to twice the rate seen with vinorelbine, consistent with the increased rescue frequency observed in cells ($P = 0.0236$ at 50 nM drug treatment; Fig. 6H). Collectively, these results indicate that DZ-2384 can directly increase the rescue frequency of dynamic microtubules, both in purified tubulin systems and in cells, suggesting that the changes to dynamic instability are related to the straightening of protofilaments induced by DZ-2384.

DISCUSSION

MTAs are part of the standard of care treatments for a wide range of cancer indications; however, there is still a need for effective but safer agents to combine with next-generation targeted therapies, including immunotherapies. A key feature of DZ-2384 is an improved safety margin (more than 24-fold versus 0.7- to 1.0-fold for vinorelbine) when comparing weight loss, clinical effects, bone marrow toxicity, and more than 13-fold considering its neurotoxicity profile. We have demonstrated that DZ-2384 has strong single-agent antitumor activity in models of pancreatic, colon, ALL, and metastatic breast cancer. The criticisms of xenograft models derived from cell lines are that they are not representative of patient tumors, they may respond differently to drugs, and the mice in which tumors are grown lack immune surveillance. We have addressed these criticisms by demonstrating that DZ-2384 is potent in multiple xenograft models, including a pancreatic PDX model, as well as a *Rgs16::GFP;KIC* GEMM model of pancreatic cancer in which the mice are immunocompetent. The results from the pancreatic models show that the DZ-2384/gemcitabine combination was more effective than gemcitabine alone, the clinical standard of care for PDA. This observation is exciting because the DZ-2384/gemcitabine combination reduced tumor initiation and progression with a superior response rate (68%) compared to the nab-paclitaxel/gemcitabine combination (53%) in the same *Rgs16::GFP;KIC* model (24). Although this latter combination is approved for the treatment of metastatic PDA, nab-paclitaxel suffers from a relatively high burden of peripheral neuropathy (39). Collectively, these results highlight DZ-2384's promise as a drug candidate for PDA and demonstrates its potential for activity in a wide range of other indications.

MTA-induced peripheral neuropathy has been linked directly to effects on axonal microtubules (40). Given that the integrity of axonal microtubules is essential for transport processes and maintaining neuromuscular junctions, it is not surprising that MTAs affect the longest nerves of the body, those innervating the feet and hands (41). DZ-2384 demonstrates no electrophysiological or microscopic signs of peripheral neuropathy at circulating DZ-2384 blood concentrations at least 13 times higher than effective antitumor concentrations in mice. However, because neurotoxicity is seen at the DZ-2384 dose of 30 mg/m^2, a potential for clinical toxicity remains at high doses. Nevertheless, in cultured primary rat neurons, the integrity of axonal microtubules was maintained in the presence of DZ-2384 compared to that in the presence of vinorelbine, suggesting a milder impact on nerve axons. Therefore, we propose that DZ-2384's improved safety margin is linked to the manner in which DZ-2384 binds to tubulin and the impact it has on microtubule integrity and dynamics.

Our crystal structure of the DZ-2384–tubulin complex and our EM data showed a pronounced straightening in the pitch and curvature of microtubule protofilaments relative to vinblastine-tubulin complexes (17). Microtubule curvature, more specifically the curvature of tubulin dimers and protofilaments, has emerged as the central theme in our current understanding of microtubule dynamic instability (11). GTP-tubulin dimers begin in the curved state, with an intradimer angle of 12° according to available crystal structures (31, 42, 43). In solution, a tubulin dimer is expected to adopt a range of conformations, with curved species predominating (44). Sometime during polymerization, the tubulin dimer

straightens as it incorporates into the microtubule lattice (12), only to return to the curved state during depolymerization when the protofilaments curve outward as “ram’s horns” (1). It is now apparent that cells control their microtubules by using MAPs that bind selectively to specific curvatures (11). Some MAPs bind to curved tubulin (43, 45), some bind to straight lattices (46), and others can force tubulin to adopt curved conformations (47).

Microtubule curvature is also an important theme in our current understanding of the mechanism of action of MTAs. Colchicine, for example, is known to trap individual tubulin dimers in the curved state (48). Vinca alkaloids bind to the longitudinal interface between two tubulin dimers, forcing the interface to adopt a curved conformation (17, 49). If the vinca alkaloid binds to this interface at the growing end of a microtubule, the affected tubulin dimers will be unable to straighten, a necessary step for their full incorporation into the microtubule lattice (11, 50). Thus, vinca alkaloids block the interdimer curved-to-straight transitions that must occur during microtubule growth, which may explain why microtubule growth is slowed at low drug concentrations (51). At high concentrations, vinca alkaloids can stabilize curved tubulin oligomers in solution (52, 53). With sufficient vinca activity, these curved oligomers may dominate, effectively sequestering tubulin into a polymerization-incompetent state. As microtubules undergo catastrophe and depolymerize, their tubulin becomes unavailable for incorporation, and in a short time, the entire microtubule cytoskeleton is depolymerized (54).

It is interesting to compare DZ-2384 to other vinca alkaloids in light of the discussion above. Both DZ-2384 and vinorelbine slow down the microtubule growth rate in vitro and in tissue culture cells. However, unlike vinorelbine, DZ-2384 increased the microtubule rescue frequency. This change in microtubule dynamics is distinct relative to other depolymerizing MTAs such as maytansine (55), cryptophycin 1 (56), dolastatin 10 (57), eribulin (58), and vincristine (59). More frequent rescues should help to rebuild microtubule polymers, which may explain why the microtubule cytoskeleton persists in DZ-2384–treated cells. Our comparison of rescue frequencies and other parameters under-reports the difference between the DZ-2384–treated and vinorelbine-treated cells. By definition, any measurement of catastrophes and rescues ignores the microtubules that are paused or that have depolymerized completely. Vinorelbine-treated cells contain fewer dynamic microtubules that could be included in the analysis than DZ-2384–treated or DMSO-treated cells (Table 2). DZ-2384’s effect on rescue frequency may result from the straightening of the interdimer interface and the decrease in the pitch of curvature. Because DZ-2384 straightens this bend, the probability that a rescue event occurs might increase. Decreases in the pitch may also facilitate lateral contacts between protofilaments during rescue events. In this way, the structural difference between DZ-2384 and other vinca alkaloids can explain the functional difference in rescue frequencies.

Together, our results demonstrate that a classic MTA binding site on tubulin can be targeted in a distinct way that results in a therapeutic agent with an unexpected lack of treatment-induced neuropathy at effective plasma concentrations. Our results provide a framework for the rational design of MTAs that deliberately alter microtubule curvature. Such changes to MTAs could confer improved pharmacological properties and broaden the scope of use of this important class of chemotherapies.

MATERIALS AND METHODS

Materials and methods are described in the Supplementary Materials.

Supplementary Material

Refer to Web version on PubMed Central for supplementary material.

Acknowledgments

We thank R. Ohi (Vanderbilt University) for the GFP–α-tubulin–expressing LLC-PK1 cells, A. Bird (MPI Dortmund) for the U-2 OS cells expressing EB3-mCherry, and J. Massagué (Memorial Sloan Kettering) for the MDA-MB-231-LM2 cells. We thank J. Haruna for neuropathology, R. Jacobs for bone marrow pathology, J. Ouellette for electron microscope expertise, D. Ethier for fluorescence-activated cell sorting expertise, E. Küster-Schöck for confocal microscopy expertise, and O. Cleaver for access to the fluorescent dissection microscope.

Funding: This work was funded by research grants to G.C.S. and P.G.H. from Diazon Pharmaceuticals Inc., Montreal, QC, Canada. Research grant support was provided by Génome Quebec and the Quebec Consortium for Drug Discovery (CQDM) (to G.C.S.), by the Canadian Institutes for Health Research (CIHR) (MOP-137055 to G.J.B., MOP-6192 and MOP-106530 to G.C.S., and MOP-119401 to P.M.S.), by the Swiss National Science Foundation (31003A_166608 to M.O.S.), and by the National Cancer Institute (NCI_CA192381 to T.M.W.), and G.Z. was supported by the Fonds de recherche du Québec–Santé clinician-scientist salary award. G.J.B. is a CIHR New Investigator.

REFERENCES AND NOTES

1. Mandelkow EM, Mandelkow E, Milligan RA. Microtubule dynamics and microtubule caps: A time-resolved cryo-electron microscopy study. J Cell Biol. 1991; 114:977–991. [PubMed: 1874792]
2. Wang HW, Nogales E. Nucleotide-dependent bending flexibility of tubulin regulates microtubule assembly. Nature. 2005; 435:911–915. [PubMed: 15959508]
3. Jordan MA, Wilson L. Microtubules as a target for anticancer drugs. Nat Rev Cancer. 2004; 4:253–265. [PubMed: 15057285]
4. Castedo M, Perfettini JL, Roumier T, Andreau K, Medema R, Kroemer G. Cell death by mitotic catastrophe: A molecular definition. Oncogene. 2004; 23:2825–2837. [PubMed: 15077146]
5. Musacchio A, Hardwick KG. The spindle checkpoint: Structural insights into dynamic signalling. Nat Rev Mol Cell Biol. 2002; 3:731–741. [PubMed: 12360190]
6. Monzó M, Rosell R, Sánchez JJ, Lee JS, O'Brate A, González-Larriba JL, Alberola V, Lorenzo JC, Núñez L, Ro JY, Martín C. Paclitaxel resistance in non-small-cell lung cancer associated with beta-tubulin gene mutations. J Clin Oncol. 1999; 17:1786–1793. [PubMed: 10561216]
7. Quasthoff S, Hartung HP. Chemotherapy-induced peripheral neuropathy. J Neurol. 2002; 249:9–17. [PubMed: 11954874]
8. Park SB, Krishnan AV, Lin CSY, Goldstein D, Friedlander M, Kiernan MC. Mechanisms underlying chemotherapy-induced neurotoxicity and the potential for neuroprotective strategies. Curr Med Chem. 2008; 15:3081–3094. [PubMed: 19075655]
9. Persohn E, Canta A, Schoepfer S, Traebert M, Mueller L, Gilardini A, Galbiati S, Nicolini G, Scuteri A, Lanzani F, Giussani G, Cavaletti G. Morphological and morphometric analysis of paclitaxel and docetaxel-induced peripheral neuropathy in rats. Eur J Cancer. 2005; 41:1460–1466. [PubMed: 15913989]
10. Han Y, Smith MT. Pathobiology of cancer chemotherapy-induced peripheral neuropathy (CIPN). Front Pharmacol. 2013; 4:156. [PubMed: 24385965]
11. Brouhard GJ, Rice LM. The contribution of αβ-tubulin curvature to microtubule dynamics. J Cell Biol. 2014; 207:323–334. [PubMed: 25385183]
12. Rice LM, Montabana EA, Agard DA. The lattice as allosteric effector: Structural studies of αβ- and γ-tubulin clarify the role of GTP in microtubule assembly. Proc Natl Acad Sci USA. 2008; 105:5378–5383. [PubMed: 18388201]

13. Dogterom M, Leibler S. Physical aspects of the growth and regulation of microtubule structures. Phys Rev Lett. 1993; 70:1347–1350. [PubMed: 10054353]
14. Walker RA, O'Brien ET, Pryer NK, Soboeiro MF, Voter WA, Erickson HP, Salmon ED. Dynamic instability of individual microtubules analyzed by video light microscopy: Rate constants and transition frequencies. J Cell Biol. 1988; 107:1437–1448. [PubMed: 3170635]
15. Desai A, Mitchison TJ. Microtubule polymerization dynamics. Annu Rev Cell Dev Biol. 1997; 13:83–117. [PubMed: 9442869]
16. Prota AE, Bargsten K, Zurwerra D, Field JJ, Diaz JF, Altmann KH, Steinmetz MO. Molecular mechanism of action of microtubule-stabilizing anticancer agents. Science. 2013; 339:587–590. [PubMed: 23287720]
17. Gigant B, Wang C, Ravelli RBG, Roussi F, Steinmetz MO, Curmi PA, Sobel A, Knossow M. Structural basis for the regulation of tubulin by vinblastine. Nature. 2005; 435:519–522. [PubMed: 15917812]
18. Lindquist N, Fenical W, Van Duyne GD, Clardy J. Isolation and structure determination of diazonamides A and B, unusual cytotoxic metabolites from the marine ascidian Diazona chinensis. J Am Chem Soc. 1991; 113:2303–2304.
19. Li J, Burgett AWG, Esser L, Amezcua C, Harran PG. Total synthesis of nominal diazonamides—Part 2: On the true structure and origin of natural isolates. Angew Chem Int Ed Engl. 2001; 40:4770–4773. [PubMed: 12404412]
20. Williams NS, Burgett AWG, Atkins AS, Wang X, Harran PG, McKnight SL. Therapeutic anticancer efficacy of a synthetic diazonamide analog in the absence of overt toxicity. Proc Natl Acad Sci USA. 2007; 104:2074–2079. [PubMed: 17287337]
21. Ding H, DeRoy PL, Perreault C, Larivée A, Siddiqui A, Caldwell CG, Harran S, Harran PG. Electrolytic macrocyclizations: Scalable synthesis of a diazonamide-based drug development candidate. Angew Chem Int Ed Engl. 2015; 54:4818–4822. [PubMed: 25729008]
22. Minn AJ, Gupta GP, Siegel PM, Bos PD, Shu W, Giri DD, Viale A, Olshen AB, Gerald WL, Massague J. Genes that mediate breast cancer metastasis to lung. Nature. 2005; 436:518–524. [PubMed: 16049480]
23. Gong J, Tuli R, Shinde A, Hendifar AE. Meta-analyses of treatment standards for pancreatic cancer. Mol Clin Oncol. 2016; 4:315–325. [PubMed: 26998283]
24. Ocal O, Pashkov V, Kollipara RK, Zolghadri Y, Cruz VH, Hale MA, Heath BR, Artyukhin AB, Christie AL, Tsoulfas P, Lorens JB, Swift GH, Brekken RA, Wilkie TM. A rapid in vivo screen for pancreatic ductal adenocarcinoma therapeutics. Dis Model Mech. 2015; 8:1201–1211. [PubMed: 26438693]
25. Dumontet C, Jordan MA. Microtubule-binding agents: A dynamic field of cancer therapeutics. Nat Rev Drug Discov. 2010; 9:790–803. [PubMed: 20885410]
26. Windebank AJ, Grisold W. Chemotherapy-induced neuropathy. J Peripher Nerv Syst. 2008; 13:27–46. [PubMed: 18346229]
27. Wang G, Shang L, Burgett AWG, Harran PG, Wang X. Diazonamide toxins reveal an unexpected function for ornithine δ-amino transferase in mitotic cell division. Proc Natl Acad Sci USA. 2007; 104:2068–2073. [PubMed: 17287350]
28. Cruz-Monserrate Z, Vervoort HC, Bai R, Newman DJ, Howell SB, Los G, Mullaney JT, Williams MD, Pettit GR, Fenical W, Hamel E. Diazonamide A and a synthetic structural analog: Disruptive effects on mitosis and cellular microtubules and analysis of their interactions with tubulin. Mol Pharmacol. 2003; 63:1273–1280. [PubMed: 12761336]
29. Prota AE, Magiera MM, Kuijpers M, Bargsten K, Frey D, Wieser M, Jaussi R, Hoogenraad CC, Kammerer RA, Janke C, Steinmetz MO. Structural basis of tubulin tyrosination by tubulin tyrosine ligase. J Cell Biol. 2013; 200:259–270. [PubMed: 23358242]
30. Liu YM, Chen HL, Lee HY, Liou JP. Tubulin inhibitors: A patent review. Expert Opin Ther Pat. 2013; 24:69–88. [PubMed: 24313741]
31. Nawrotek A, Knossow M, Gigant B. The determinants that govern microtubule assembly from the atomic structure of GTP-tubulin. J Mol Biol. 2011; 412:35–42. [PubMed: 21787788]
32. Lobert S, Ingram JW, Correia JJ. The thermodynamics of vinca alkaloid-induced tubulin spirals formation. Biophys Chem. 2007; 126:50–58. [PubMed: 16757093]

33. Vassilev LT, Tovar C, Chen S, Knezevic D, Zhao X, Sun H, Heimbrook DC, Chen L. Selective small-molecule inhibitor reveals critical mitotic functions of human CDK1. Proc Natl Acad Sci USA. 2006; 103:10660–10665. [PubMed: 16818887]
34. Matov A, Applegate K, Kumar P, Thoma C, Krek W, Danuser G, Wittmann T. Analysis of microtubule dynamic instability using a plus-end growth marker. Nat Methods. 2010; 7:761–768. [PubMed: 20729842]
35. Rusan NM, Fagerstrom CJ, Yvon AMC, Wadsworth P. Cell cycle-dependent changes in microtubule dynamics in living cells expressing green fluorescent protein-a tubulin. Mol Biol Cell. 2001; 12:971–980. [PubMed: 11294900]
36. Gell C, Bormuth V, Brouhard GJ, Cohen DN, Diez S, Friel CT, Helenius J, Nitzsche B, Petzold H, Ribbe J, Schäffer E, Stear JH, Trushko A, Varga V, Widlund PO, Zanic M, Howard J. Microtubule dynamics reconstituted in vitro and imaged by single-molecule fluorescence microscopy. Methods Cell Biol. 2010; 95:221–245. [PubMed: 20466138]
37. Ngan VK, Bellman K, Panda D, Hill BT, Jordan MA, Wilson L. Novel actions of the antitumor drugs vinflunine and vinorelbine on microtubules. Cancer Res. 2000; 60:5045–5051. [PubMed: 11016627]
38. Mohan R, Katrukha EA, Doodhi H, Smal I, Meijering E, Kapitein LC, Steinmetz MO, Akhmanova A. End-binding proteins sensitize microtubules to the action of microtubule-targeting agents. Proc Natl Acad Sci USA. 2013; 110:8900–8905. [PubMed: 23674690]
39. Peng L, Bu Z, Ye X, Zhou Y, Zhao Q. Incidence and risk of peripheral neuropathy with nab-paclitaxel in patients with cancer: A meta-analysis. Eur J Cancer Care. 2015
40. Argyriou AA, Bruna J, Marmiroli P, Cavaletti G. Chemotherapy-induced peripheral neurotoxicity (CIPN): An update. Crit Rev Oncol Hematol. 2012; 82:51–77. [PubMed: 21908200]
41. Komlodi-Pasztor E, Sackett D, Wilkerson J, Fojo T. Mitosis is not a key target of microtubule agents in patient tumors. Nat Rev Clin Oncol. 2011; 8:244–250. [PubMed: 21283127]
42. Pecqueur L, Duellberg C, Dreier B, Jiang Q, Wang C, Plückthun A, Surrey T, Gigant B, Knossow M. A designed ankyrin repeat protein selected to bind to tubulin caps the microtubule plus end. Proc Natl Acad Sci USA. 2012; 109:12011–12016. [PubMed: 22778434]
43. Ayaz P, Ye X, Huddleston P, Brautigam CA, Rice LM. A TOG:αβ-tubulin complex structure reveals conformation-based mechanisms for a microtubule polymerase. Science. 2012; 337:857–860. [PubMed: 22904013]
44. Peng LX, Hsu MT, Bonomi M, Agard DA, Jacobson MP. The free energy profile of tubulin straight-bent conformational changes, with implications for microtubule assembly and drug discovery. PLOS Comput Biol. 2014; 10:e1003464. [PubMed: 24516374]
45. Bechstedt S, Lu K, Brouhard GJ. Doublecortin recognizes the longitudinal curvature of the microtubule end and lattice. Curr Biol. 2014; 24:2366–2375. [PubMed: 25283777]
46. Alushin GM, Ramey VH, Pasqualato S, Ball DA, Grigorieff N, Musacchio A, Nogales E. The Ndc80 kinetochore complex forms oligomeric arrays along microtubules. Nature. 2010; 467:805–810. [PubMed: 20944740]
47. Desai A, Verma S, Mitchison TJ, Walczak CE. Kin I kinesins are microtubule-destabilizing enzymes. Cell. 1999; 96:69–78. [PubMed: 9989498]
48. Ravelli RBG, Gigant B, Curmi PA, Jourdain I, Lachkar S, Sobel A, Knossow M. Insight into tubulin regulation from a complex with colchicine and a stathmin-like domain. Nature. 2004; 428:198–202. [PubMed: 15014504]
49. Wilson L, Jordan MA, Morse A, Margolis RL. Interaction of vinblastine with steady-state microtubules in vitro. J Mol Biol. 1982; 159:125–149. [PubMed: 7131559]
50. Alushin GM, Lander GC, Kellogg EH, Zhang R, Baker D, Nogales E. High-resolution microtubule structures reveal the structural transitions in αβ-tubulin upon GTP hydrolysis. Cell. 2014; 157:1117–1129. [PubMed: 24855948]
51. Toso RJ, Jordan MA, Farrell KW, Matsumoto B, Wilson L. Kinetic stabilization of microtubule dynamic instability in vitro by vinblastine. Biochemistry. 1993; 32:1285–1293. [PubMed: 8448138]
52. Himes RH. Interactions of the catharanthus (Vinca) alkaloids with tubulin and microtubules. Pharmacol Ther. 1991; 51:257–267. [PubMed: 1784631]

53. Weisenberg RC, Timasheff SN. Aggregation of microtubule subunit protein. Effects of divalent cations, colchicine and vinblastine. Biochemistry. 1970; 9:4110–4116. [PubMed: 5458644]
54. Belmont LD, Mitchison TJ. Identification of a protein that interacts with tubulin dimers and increases the catastrophe rate of microtubules. Cell. 1996; 84:623–631. [PubMed: 8598048]
55. Lopus M, Oroudjev E, Wilson L, Wilhelm S, Widdison W, Chari R, Jordan MA. Maytansine and cellular metabolites of antibody-maytansinoid conjugates strongly suppress microtubule dynamics by binding to microtubules. Mol Cancer Ther. 2010; 9:2689–2699. [PubMed: 20937594]
56. Panda D, Himes RH, Moore RE, Wilson L, Jordan MA. Mechanism of action of the unusually potent microtubule inhibitor cryptophycin 1. Biochemistry. 1997; 36:12948–12953. [PubMed: 9335554]
57. Gajula PK, Asthana J, Panda D, Chakraborty TK. A synthetic dolastatin 10 analogue suppresses microtubule dynamics, inhibits cell proliferation, and induces apoptotic cell death. J Med Chem. 2013; 56:2235–2245. [PubMed: 23445405]
58. Jordan MA, Kamath K, Manna T, Okouneva T, Miller HP, Davis C, Littlefield BA, Wilson L. The primary antimitotic mechanism of action of the synthetic halichondrin E7389 is suppression of microtubule growth. Mol Cancer Ther. 2005; 4:1086–1095. [PubMed: 16020666]
59. Gan PP, McCarroll JA, Po'uha ST, Kamath K, Jordan MA, Kavallaris M. Microtubule dynamics, mitotic arrest, and apoptosis: Drug-induced differential effects of βIII-tubulin. Mol Cancer Ther. 2010; 9:1339–1348. [PubMed: 20442307]
60. Ranaivoson FM, Gigant B, Berritt S, Joullié M, Knossow M. Structural plasticity of tubulin assembly probed by vinca-domain ligands. Acta Crystallogr Sect D Biol Crystallogr. 2012; 68:927–934. [PubMed: 22868758]
61. Waight AB, Bargsten K, Doronina S, Steinmetz MO, Sussman D, Prota AE. Structural basis of microtubule destabilization by potent auristatin anti-mitotics. PLOS ONE. 2016; 11:e0160890. [PubMed: 27518442]
62. Gardner MK, Charlebois BD, Jánosi IM, Howard J, Hunt AJ, Odde DJ. Rapid microtubule self-assembly kinetics. Cell. 2011; 146:582–592. [PubMed: 21854983]
63. Smith AL, Bascuñana C, Hall A, Salman A, Andrei AZ, Volenik A, Rothenmund H, Ferland D, Lamoussenery D, Kamath AS, Amre R, Caglar D, Gao ZH, Haegert DG, Kanber Y, Michel RP, Omeroglu-Altinel G, Asselah J, Bouganim N, Kavan P, Arena G, Barkun J, Chaudhury P, Gallinger S, Foulkes WD, Omeroglu A, Metrakos P, Zogopoulos G. Establishing a clinic-based pancreatic cancer and periampullary tumour research registry in Quebec. Curr Oncol. 2015; 22:113–121. [PubMed: 25908910]
64. Holmfeldt L, Mullighan CG. Generation of human acute lymphoblastic leukemia xenografts for use in oncology drug discovery. Curr Protoc Pharmacol. 2015; 68:14.32.1–14.32.19. [PubMed: 25737157]
65. Jang WI, Lin ZL, Lee SH, Namgoong S, Kim NH. A specific inhibitor of CDK1, RO-3306, reversibly arrests meiosis during in vitro maturation of porcine oocytes. Anim Reprod Sci. 2014; 144:102–108. [PubMed: 24374180]
66. Shang E, Wang X, Wen D, Greenberg DA, Wolgemuth DJ. Double bromodomain-containing gene *Brd2* is essential for embryonic development in mouse. Dev Dyn. 2009; 238:908–917. [PubMed: 19301389]
67. Tae HS, Hines J, Schneekloth AR, Crews CM. Total synthesis and biological evaluation of tyroscherin. Org Lett. 2010; 12:4308–4311. [PubMed: 20831175]
68. Fráter G, Müller U, Kraft P. On the scope of a *Prins*-type cyclization of oxonium ions. Helv Chim Acta. 2004; 87:2750–2763.
69. Bartlett PA, Tanzella DJ, Barstow JF. Ester-enolate claisen rearrangement of lactic acid derivatives. J Org Chem. 1982; 47:3941–3945.
70. Kabsch W. XDS. Acta Crystallogr Sect D Biol Crystallogr. 2010; 66:125–132. [PubMed: 20124692]
71. Adams PD, Afonine PV, Bunkóczi G, Chen VB, Davis IW, Echols N, Headd JJ, Hung L-W, Kapral GJ, Grosse-Kunstleve RW, McCoy AJ, Moriarty NW, Oeffner R, Read RJ, Richardson DC, Richardson JS, Terwilliger TC, Zwart PH. *PHENIX*: A comprehensive Python-based system for

macromolecular structure solution. Acta Crystallogr Sect D Biol Crystallogr. 2010; 66:213–221. [PubMed: 20124702]

72. Emsley P, Cowtan K. *Coot*: Model-building tools for molecular graphics. Acta Crystallogr Sect D Biol Crystallogr. 2004; 60:2126–2132. [PubMed: 15572765]
73. Hari M, Loganzo F, Annable T, Tan X, Musto S, Morilla DB, Nettles JH, Snyder JP, Greenberger LM. Paclitaxel-resistant cells have a mutation in the paclitaxel-binding region of β-tubulin ($Asp^{26}Glu$) and less stable microtubules. Mol Cancer Ther. 2006; 5:270–278. [PubMed: 16505100]
74. Castoldi M, Popov AV. Purification of brain tubulin through two cycles of polymerization-depolymerization in a high-molarity buffer. Protein Expr Purif. 2003; 32:83–88. [PubMed: 14680943]
75. Hyman A, Drechsel D, Kellogg D, Salser S, Sawin K, Steffen P, Wordeman L, Mitchison T. Preparation of modified tubulins. Methods Enzymol. 1991; 196:478–485. [PubMed: 2034137]
76. Helenius J, Brouhard G, Kalaidzidis Y, Diez S, Howard J. The depolymerizing kinesin MCAK uses lattice diffusion to rapidly target microtubule ends. Nature. 2006; 441:115–119. [PubMed: 16672973]
77. Bechstedt S, Brouhard GJ. Doublecortin recognizes the 13-protofilament microtubule cooperatively and tracks microtubule ends. Dev Cell. 2012; 23:181–192. [PubMed: 22727374]

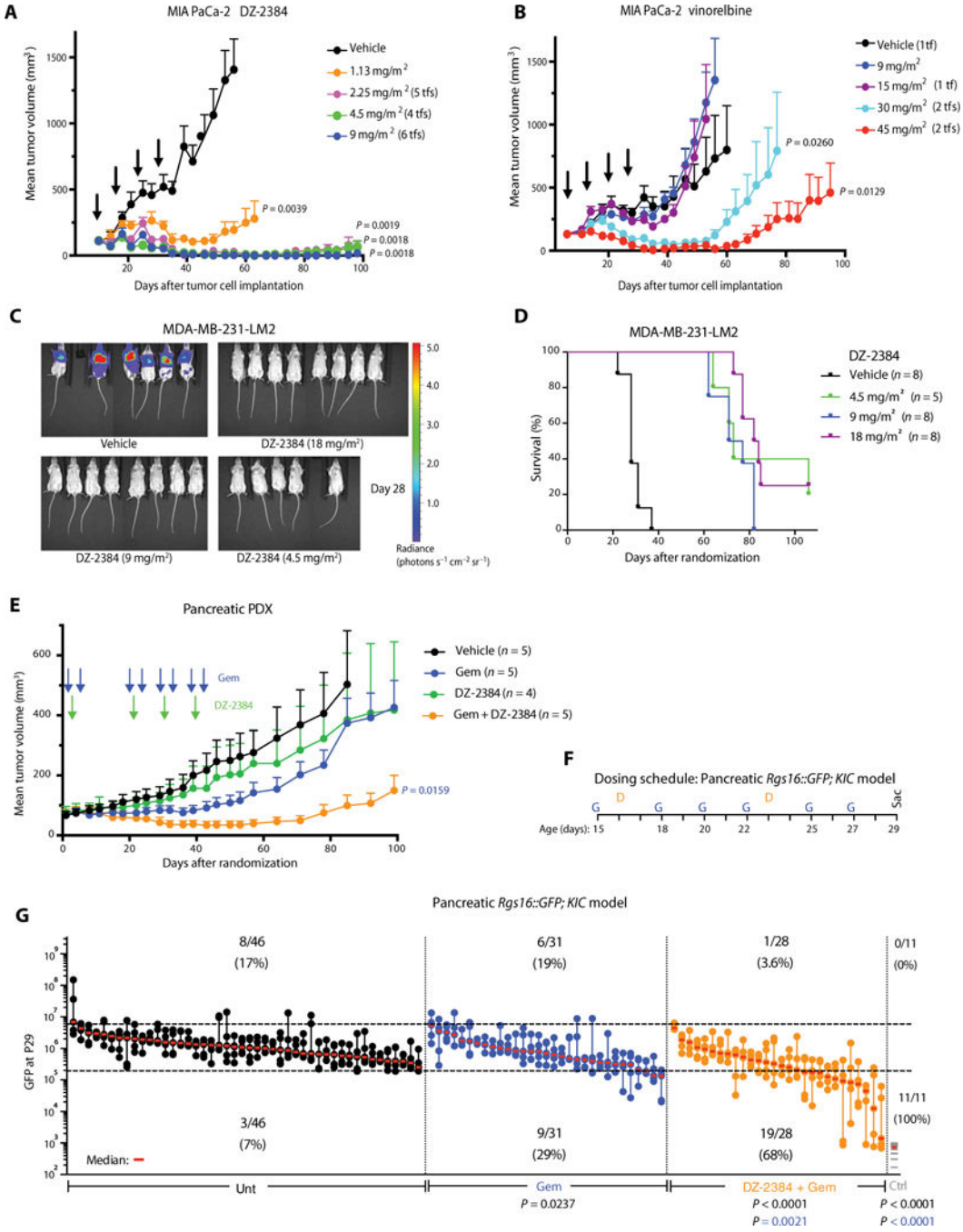

Fig. 1. DZ-2384 has potent antitumor activity as a single agent and in combination with gemcitabine

(**A** and **B**) Mean volume of MIA PaCa-2 tumors after 4 weeks of weekly bolus intravenous administrations (indicated by arrows) of vehicle, DZ-2384 (**A**), or vinorelbine (**B**). Error bars represent means ± SEM, $n = 6$. Tf, number of tumor-free animals on day 95. *P* values were determined on day 53. (**C**) In vivo bioluminescent imaging of luciferase-expressing MDA-MB-231-LM2 breast cancer metastases in the lungs is presented as a pseudocolor heat map of photon flux on day 28 after treatment initiation. (**D**) Kaplan-Meier curves

representing survival of mice with MDA-MB-231-LM2 breast cancer metastases to the lung. *P* values <0.0001 for all treated mice were calculated using the log-rank (Mantel-Cox) test relative to vehicle-treated mice. (**E**) Mean tumor volume of a human pancreatic cancer PDX after treatment with gemcitabine (Gem) (100 mg/m^2) or DZ-2384 (36 mg/m^2) alone or in combination according to the schedule indicated by arrows. Error bars represent means ± SEM, $n = 5$. *P* values were determined on day 92. (**F**) Treatment schedule for the *Rgs16::GFP;KIC* pancreatic model: DZ-2384 (7.5 and 30 mg/m^2 for the first and second injection on P16 and P23, respectively) and gemcitabine (37.5 mg/m^2 three times weekly as indicated). (**G**) Maximum tumor burden (GFP) signal of untreated (Unt; $n = 46$), gemcitabine-treated ($n = 31$), or gemcitabine + DZ-2384–treated ($n = 28$) groups of mice on P29 is represented quantitatively. Each aligned vertical dot column represents one pancreas, and dots are the first to fifth brightest nonoverlapping pancreas fields; the median is in red. GFP expression in *Rgs16::GFP; non-KIC* control (Ctrl) mice is represented by one gray line per mouse. Top and bottom dashed horizontal lines mark the 95th and 1st percentile, respectively, of all untreated animal GFP values. Numbers below the 1st percentile represent the mildly or nontumorigenic pancreatic fields, and comparison with untreated animals represents the response rate (indicated below the bottom dashed line). All *P* values except in (D) were determined by Student's unpaired two-tailed *t* test with Welch's correction; the color matches the comparison group.

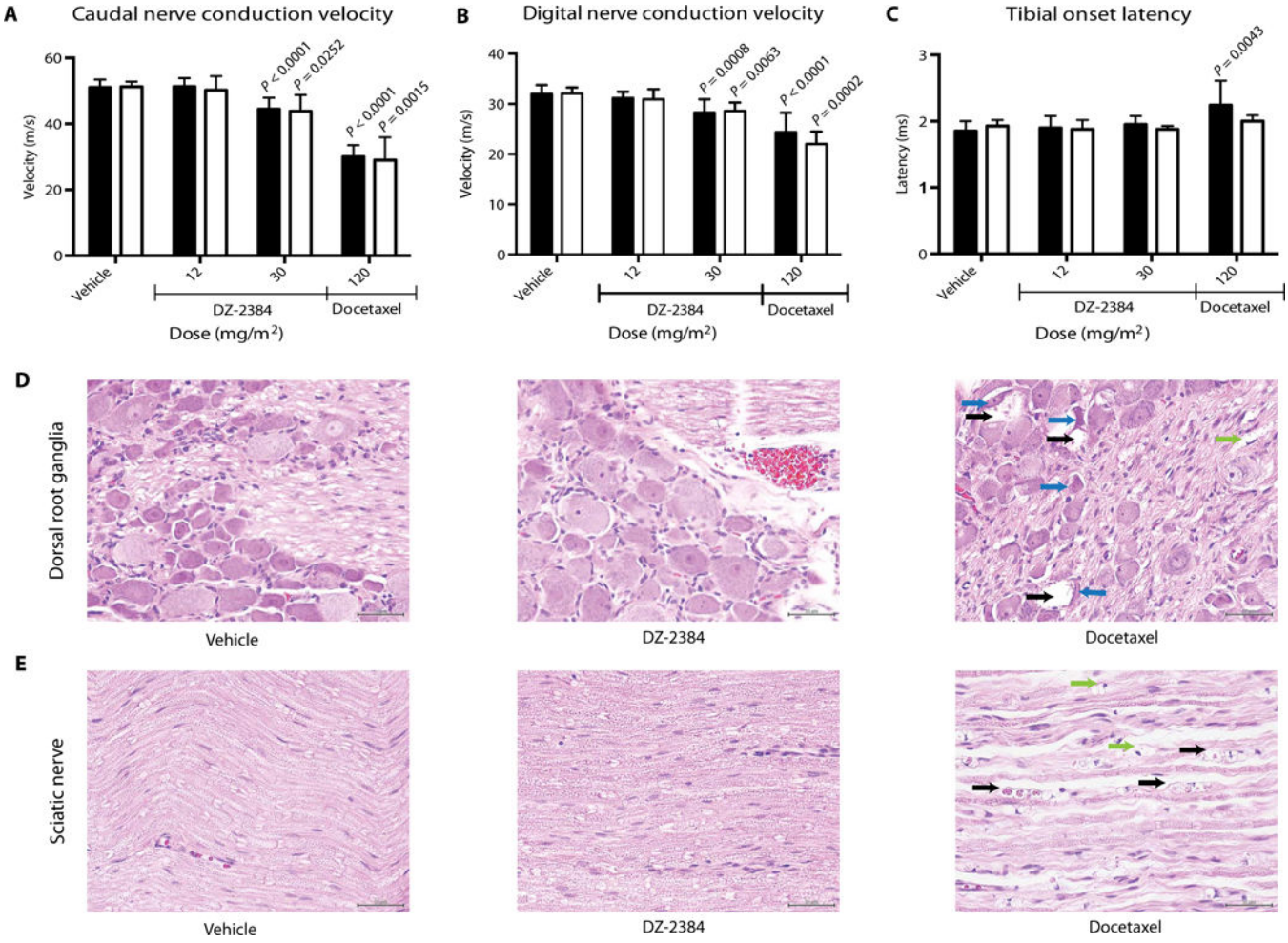

Fig. 2. DZ-2384 has no effects on NCV, latency, and histopathology at effective antitumor concentrations

(**A** to **C**) Electrophysiological parameters were measured on caudal (A), digital (B), and tibial (C) nerves. Black bars represent measurements taken on day 24 after four weekly administrations of DZ-2384 or docetaxel at the doses indicated ($n = 12$). White bars represent measurements taken on day 44, allowing a 22-day recovery as indicated ($n = 5$). Error bars represent SD. *P* values were determined using an unpaired nonparametric Student's t test. Each *P* value indicated is compared to vehicle bars of the corresponding color. (**D** and **E**) Histopathology of dorsal root ganglia (D) and sciatic nerve (E) tissue sections taken at necropsy on day 44. Arrows denote degenerating neurons with vacuolated cytoplasm (black) and condensed nuclei (blue). Black arrows in the sciatic nerve denote degenerating axons. Green arrows in the dorsal root ganglia and sciatic nerve denote digestion chambers. Scale bars, 50 μm.

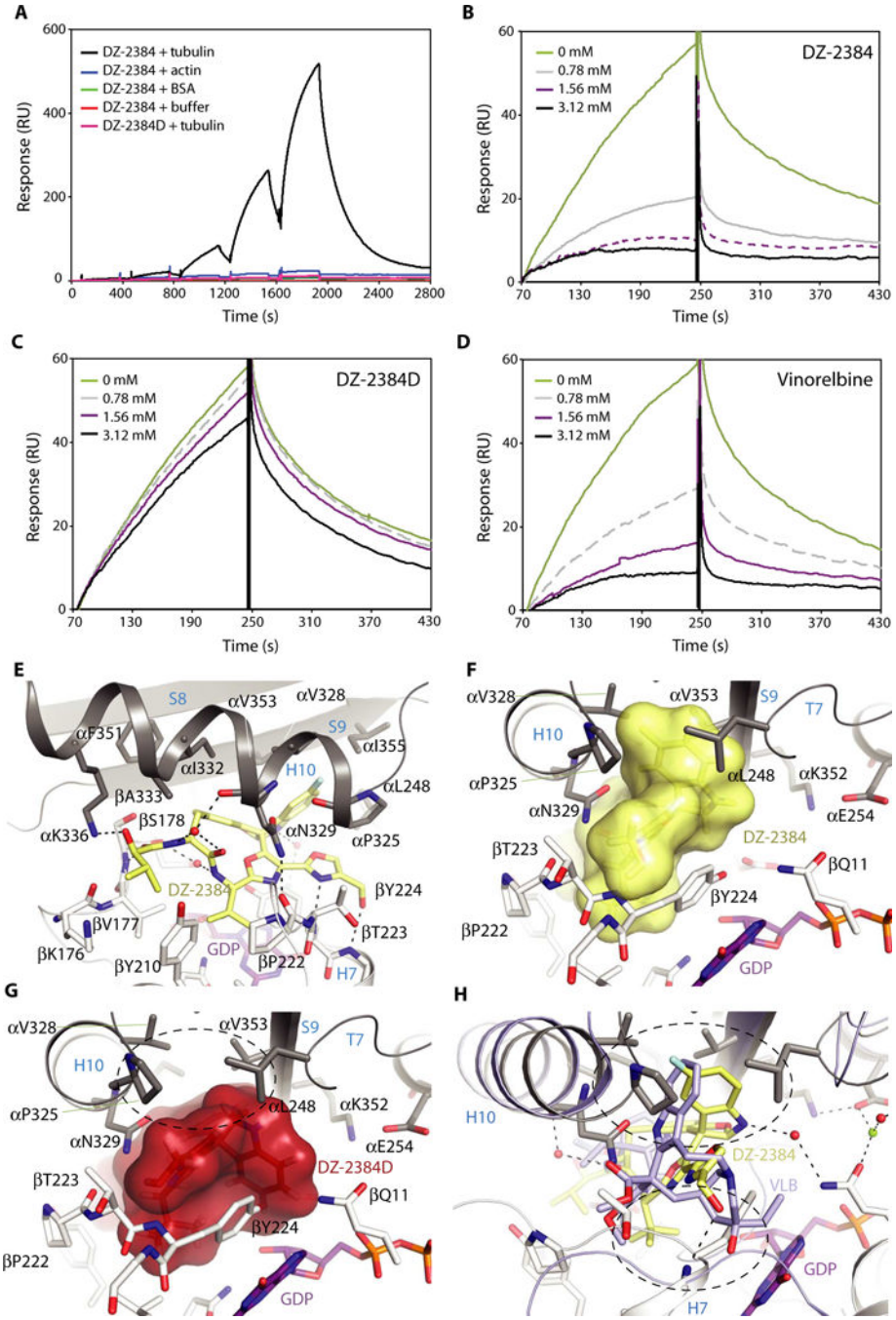

Fig. 3. DZ-2384 binds to the vinca domain of tubulin

(**A**) Specific, dose-dependent binding of tubulin dimers to DZ-2384 as assessed by SPR in single-cycle mode. Buffer (red), BSA (green), actin (blue), and tubulin (black) were titrated (0 to 10 mM; twofold dilution series) over biotinylated DZ-2384 [200 resonance units (RUs) immobilized]; under similar conditions, tubulin was titrated over biotinylated DZ-2384D surfaces (pink). (**B** to **D**) Multi-cycle SPR experiments in which the interaction between tubulin (3 μM) and DZ-2384 (biotin-immobilized) was tested in the presence of nonbiotinylated DZ-2384 (B), DZ-2384D (C), and vinorelbine (D) competitors at the concentrations

indicated. (E) Closeup view of the interaction between DZ-2384 (yellow sticks) and tubulin (gray and white ribbon). Interacting residues of α- and β-tubulin are shown in gray and white stick representation and are labeled. Hydrogen bonds are highlighted as dashed black lines. Secondary structural elements are labeled in blue. GDP, guanosine diphosphate. (F) View into the binding site turned by 90°. The ligand DZ-2384 is in yellow surface representation. The same display settings as in (E) are applied. (G) Surface representation of the inactive DZ-2384D diastereomer after modeling it into the DZ-2384 binding site. The hydrophobic pocket that interacts with the indoline moiety of DZ-2384 is devoid of any interaction in the case of the inactive compound (dashed black circle). (H) Superposition of the DZ-2384 (yellow) and vinblastine (VLB) [blue; PDB ID 4EB6 (60)] crystal structures. The top dashed circle indicates the hydrophobic pocket in α-tubulin that is occupied by the indoline moieties of both compounds in their complexes with tubulin. The bottom dashed circle highlights the bulky catharanthine moiety of vinblastine that is missing in DZ-2384.

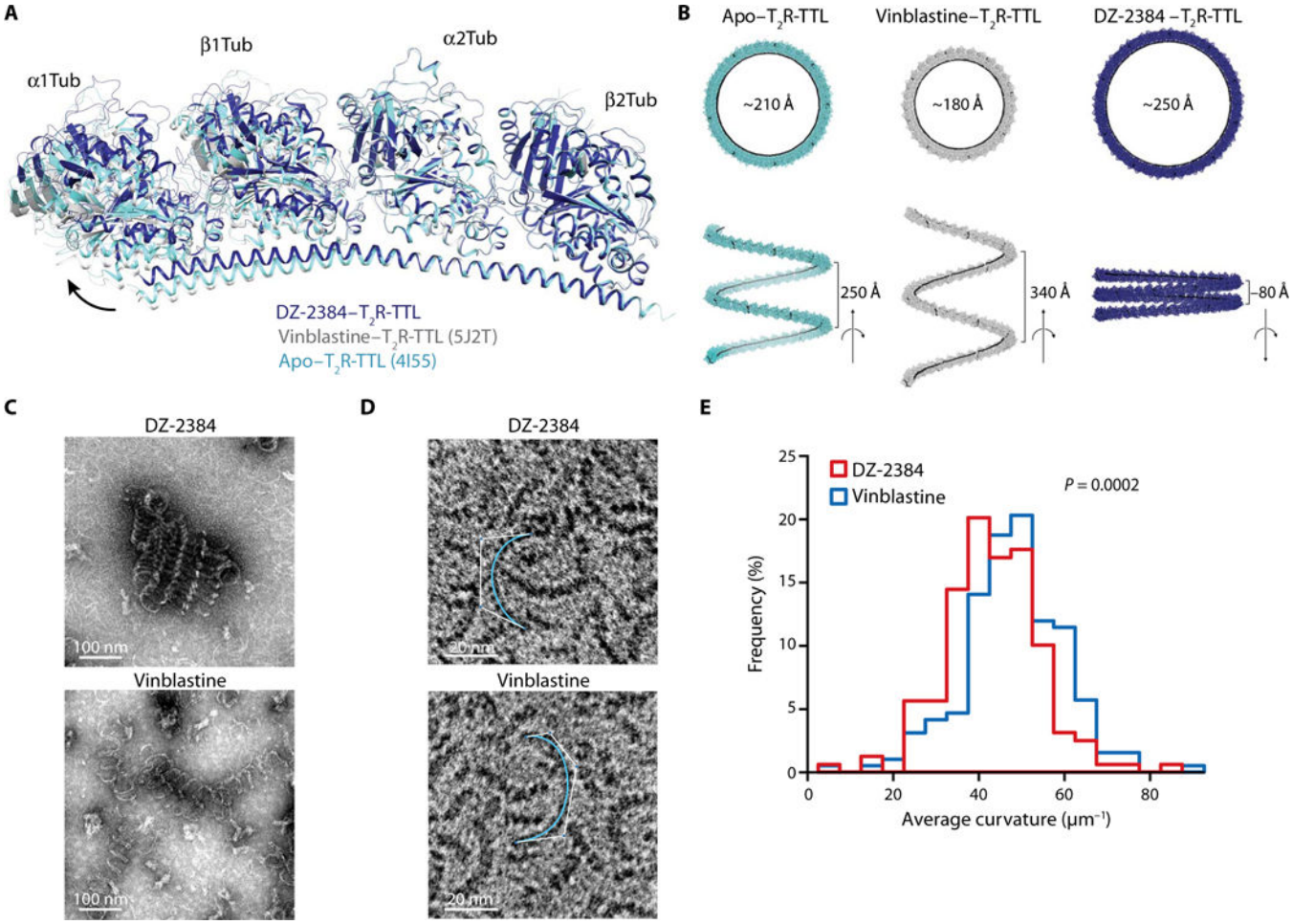

Fig. 4. DZ-2384 affects tubulin dimer curvature

(**A**) Ribbon diagram outlining the proposed difference in relative orientation between αβ-tubulin dimers in apo–T_2R-TTL [aquamarine ribbon; PDB ID 4I55 (16)] compared to T_2R-TTL complexed with vinblastine [gray ribbon; PDB ID 5J2T (61)] or DZ-2384 (blue ribbon). (**B**) Variation of the relative orientation of tubulin heterodimers in the different T_2R-TTL complexes displayed in (A). Shown are models of helical oligomers obtained from the repetition of the indicated T_2R-TTL complexes. The resulting helices are viewed along (bottom) and perpendicular (top) to their axes. Values for radii and pitches are given in black. (**C** and **D**) Electron micrographs of negatively stained MAP-rich (C) or purified (D) tubulin oligomers formed with 10 μM DZ-2384 (top) or 10 μM vinblastine (bottom). Curves used to quantitate oligomer curvature are shown in aquamarine (D). (**E**) Histogram of average curvature values for each condition [DZ-2384 (red) and vinblastine (blue)] with a bin of 5 μm^{-1} (n = 159 for DZ-2384 and n = 192 for vinblastine). P value was calculated using Welch's t test.

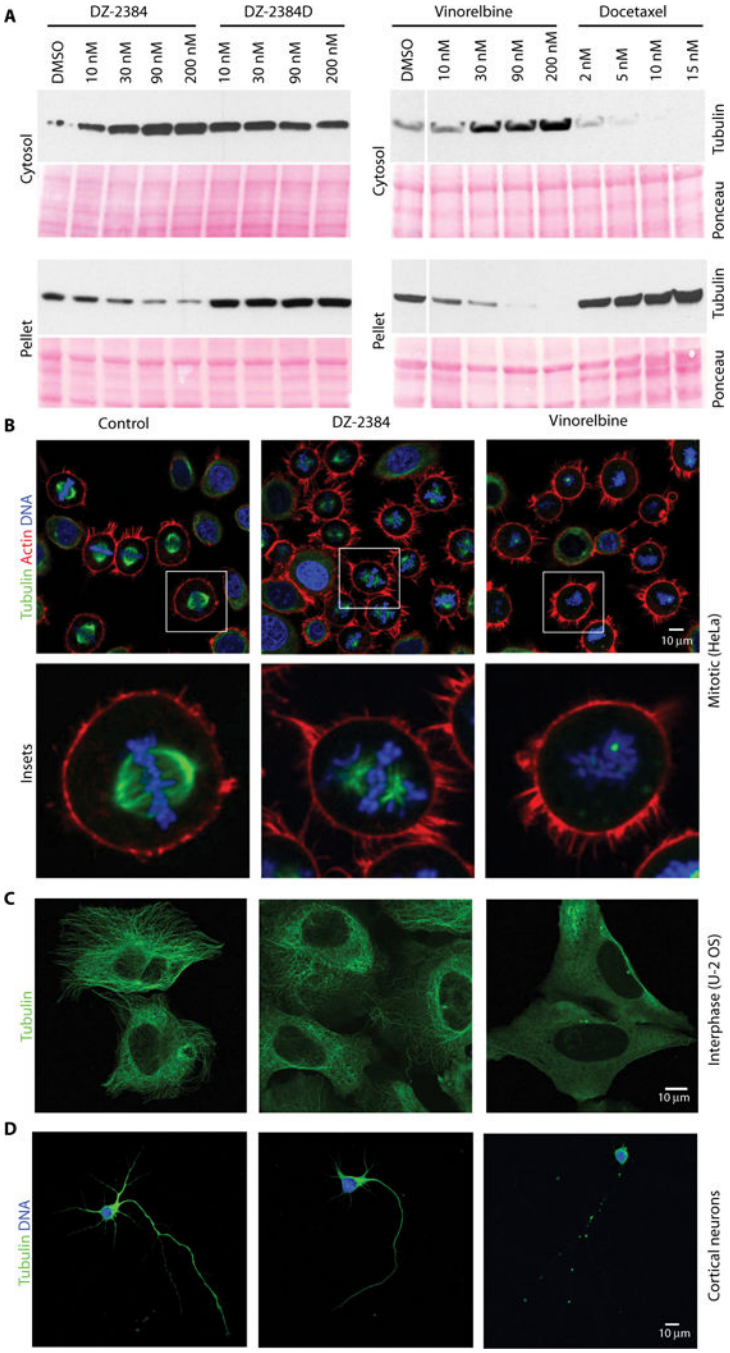

Fig. 5. DZ-2384 affects mitotic microtubules but minimally affects interphase and neuronal microtubules

(**A**) Western blot analysis of microtubule polymers (α-tubulin) isolated from H1299 cells treated with a dose range of DZ-2384, the inactive analog DZ-2384D, vinorelbine, or docetaxel for 4 hours. Ponceau staining shows equal protein loading. DMSO, dimethyl sulfoxide. (**B**) HeLa cells were synchronized with RO-3306 and then washed and released in DMSO (left) or at the IC_{80} of DZ-2384 (4 nM) (middle) and vinorel-bine (11 nM) (right) for 1 hour before fixation. Samples were immunostained with an antibody to α-tubulin (green) and phalloidin (red) and with 4′,6-diamidino-2-phenylindole (DAPI) (blue). Images were

acquired by confocal microscopy with a 40× objective. Insets show an enlargement of single cells (bottom). (**C**) Non-synchronized U-2 osteosarcoma (OS) cells treated for 2 hours with the IC_{80} of each compound (300 nM each) and then immunostained with an α-tubulin antibody (green). (**D**) Treatment of E18 rat primary cortical neurons with 10 nM DZ-2384 or vinorelbine for 1 hour (IC_{50} values for DZ2384 and vinorelbine were 43 and 68 nM, respectively). Cells are immunostained with an α-tubulin antibody (green), and nuclei are stained with DAPI (blue).

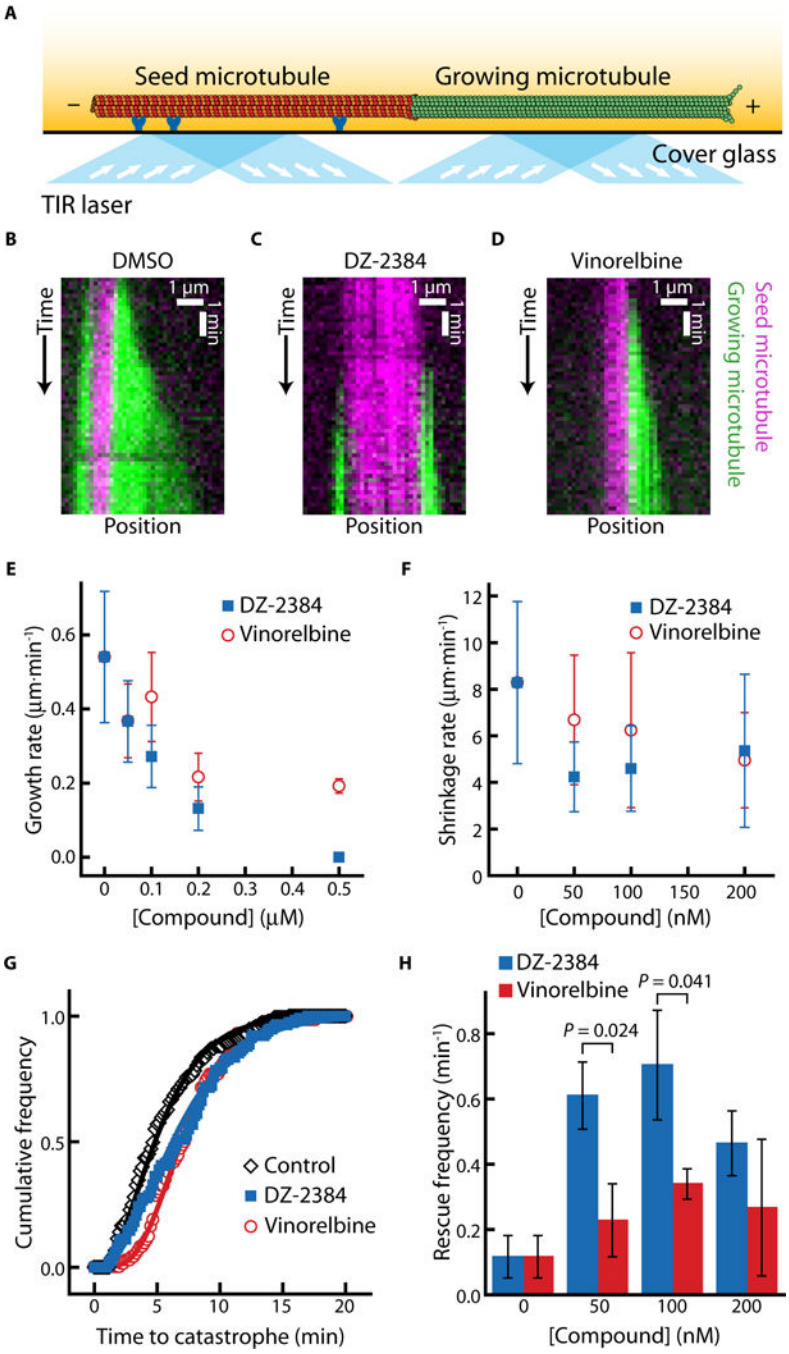

Fig. 6. DZ-2384 and vinorelbine affect microtubule dynamics differently in vitro

(**A**) Schematic of the in vitro assay for observing microtubule dynamics. The seed microtubule (red) is adhered to a cover glass surface by anti-rhodamine antibodies (dark blue). The dynamic microtubule (green) extends from the seed microtubule. Excitation by total internal reflection (TIR) lasers (light blue with arrows) allows for the observation of individual microtubules in the evanescent field (yellow fade). (**B** to **D**) Kymographs (distance versus time plot) depicting a dynamic microtubule (green) growing from a stabilized seed (magenta) in a standard polymerization buffer with DMSO [1% (v/v)] (B),

DZ-2384 (200 nM) (C), or vinorelbine (200 nM) (D). (**E**) Microtubule growth rates plotted against increasing concentrations of DZ-2384 (blue squares) or vinorelbine (red circles). (**F**) Post-catastrophe shrinkage rates plotted against increasing concentrations of DZ-2384 (blue squares) or vinorelbine (red circles). (**G**) Cumulative frequency distribution of the time until catastrophe in the presence of DZ-2384 (200 nM) (blue squares), vinorelbine (200 nM) (red circles), or in 1% (v/v) DMSO (black diamonds). Solid lines are fits to the gamma distribution, as described in (62). (**H**) Column plot of rescue frequencies at increasing concentrations of DZ-2384 (blue bars) or vinorelbine (red bars). Error bars in (E) and (F) represent SD. Data in (E) and (G) contain 74 to 193 measurements from three different experiments. Data in (F) and (H) contain 75 to 192 measurements from three different experiments. *P* values were calculated using Welch's *t* test.

Table 1

DZ-2384 has a wide therapeutic window compared to vinorelbine in mice.

Compound	Tumor model	MED*		NOAEL†		Safety margin at NOAEL‡
		Dose (mg/m^2)	Exposure§ [$AUC_{0-\alpha}$(ng·hour/ml)]	Dose (mg/m^2)	Exposure§ [$AUC_{0-\alpha}$(ng·hour/ml)]	
DZ-2384	**MIA PaCa-2**	1.13	157	36	8398	**53.5**
	HT-29	4.5	344			**24.4**
Vinorelbine	**MIA PaCa-2**	30	2309	30	2309	**1**
	HT-29	45	3380			**0.7**

*Minimum dose resulting in statistically significant antitumor activity relative to vehicle control. Calculated using mean tumor volume for MIA PaCa-2 and overall survival for HT-29 models.

†No observable adverse effect level (NOAEL): Maximum dose at which no adverse clinical signs, no body weight loss, and no effects on blood cell counts, biochemistry, and bone marrow were observed.

‡Safety margin defined as the ratio between NOAEL and MED.

§Pharmacokinetic exposure measured by circulating plasma concentration (area under the concentration-time curve, AUC).

Table 2

DZ-2384 has different effects from vinorelbine on microtubule dynamics in LLC-PK1 cells

Measurements represent the means ± SD of four independent experiments; each experiment represents at least three to five different cells for each condition. Catastrophe and rescue frequencies are presented on an overall basis (not per microtubule). *P* values were determined by an unpaired Student's *t* test with Welch's correction relative to DMSO control-treated cells. Statistically significant values are marked in bold.

Dynamic parameters	DMSO	DZ-2384* (*P*)	Vinorelbine* (*P*)
Growth			
Rate (μm/min)	12.0 ± 0.3	**8.3 ±1.6 (0.0164)**	**7.8. ± 1.5 (0.0091)**
Distance (μm)	2.8 ± 0.1	2.4 ± 0.3 (0.0631)	**2.1 ± 0.2 (0.0036)**
Duration (s)	14.8 ± 0.6	19.0 ± 6.2 (0.2666)	17.5 ± 5.8 (0.4242)
Shrink			
Rate (μm/min)	28.8 ± 3.4	27.7 ± 2.2 (0.6081)	24.6 ± 3.5 (0.1242)
Distance (μm)	5.3 ± 0.9	4.7 ± 0.9 (0.3899)	6.4 ± 1.4 (0.2345)
Duration (s)	11.4 ± 2.6	10.6 ± 1.3 (0.6087)	17.6 ± 6.6 (0.1570)
Dynamicity (μm/min)	12.8 ± 0.5	10.4 ±1.4 (0.0335)	10.2 ±1.3 (0.0165)
%**Time per phase**			
Growth	41.1 ±11.0	42.1 ± 13.1 (0.9109)	13.1 ± 7.3 (0.0074)
Shrink	28.6 ± 5.5	25.2 ± 1.4 (0.3079)	38.6 ± 8.6 (0.1068)
Pause	30.3 ± 6.5	32.7 ± 12.1 (0.7422)	48.4 ± 8.1 (0.0141)
Frequencies			
Rescue (s^{-1})	0.023 ± 0.007	0.046 ± 0.005 (0.0024)	0.017 ± 0.002 (0.1846)
Rescue (μm^{-1})	0.051 ± 0.01	0.10 ± 0.008 (0.0019)	0.043 ± 0.006 (0.3547)
Catastrophe (s^{-1})	0.025 ± 0.005	0.018 ± 0.003 (0.0619)	0.027 ± 0.003 (0.5360)
Catastrophe (μm^{-1})	0.25 ± 0.1	0.27 ± 0.1 (0.8116)	**0.97 ± 0.4 (0.0248)**
Number of microtubules	127	107	73

*Drug concentrations tested represent the IC_{80} of growth inhibition based on a 3-day viability assay and were 24 nM for DZ 23484 and 11 nM for vinorelbine.